Available online at www.sciencedirect.com
SCIENCE DIRECT®
Journal of Sound and Vibration 284 (2005) 361–378
JOURNAL OF SOUND AND VIBRATION
www.elsevier.com/locate/jsvi

Structural vibration control using spatially configured opto-electromechanical actuators

Hui-Ru Shih[a,*], Horn-Sen Tzou[b], Manov Saypuri[a]

[a]*Department of Technology, P.O. Box 18480, Jackson State University, Jackson, MS 39217, USA*
[b]*Department of Mechanical Engineering, University of Kentucky, Lexington, KY 40506, USA*

Received 14 August 2000; accepted 16 June 2004

Abstract

Traditional smart-material actuator systems are hard-wired, so that they are likely sensitive to electromagnetic interference in many operating conditions and environments. A photostrictive type of opto-electromechanical actuator activated by high-energy lights can introduce actuation and control effects without hard-wired connections. In this paper, the behavior of photostrictive opto-electromechanical actuators bonded to the surface of two-dimensional (2D) elastic structures for active vibration control is investigated. General opto-piezo-thermo-elastic equations for predicting opto-piezo-thermo-elastic behavior of photostrictive opto-electromechanical actuators are presented. All material constants of photostrictive actuators are calibrated based on laboratory experiments. Analytical solutions and numerical results demonstrate that the spatially configured discrete opto-electromechanical actuators at carefully selected locations can effectively suppress the dominating fundamental vibration modes of 2D structures.

1. Introduction

In recent years, tremendous research efforts have been focusing on active structural vibration control using traditional electromechanical transducers (such as piezoelectric, electrostrictive, and magnetostrictive actuators) [1–7]. Usually, these traditional actuators require hard-wired

*Corresponding author. Tel.: +1-601-979-2520; fax: +1-601-979-4110.
E-mail addresses: huiru.shih@jsums.edu (H.-R. Shih), hstzou@engr.uky.edu (H.-S. Tzou).

0022-460X/$ - see front matter © 2004 Elsevier Ltd. All rights reserved.
doi:10.1016/j.jsv.2004.06.013

connections to transmit the control signals. Due to the existence of external electromagnetic field in many operating environments, often there is electromagnetic interference using the traditional electromechanical transducers. In order to remedy this problem, optically driven distributed opto-electromechanical actuators, which can provide actuation without hard wires, need to be developed.

Photostrictive material is capable of producing a strain on its surface in response to a high−intensity light. The feasibility and the performance of the photostrictive type of actuator applied to one-dimensional systems have been demonstrated by a number of researchers [8–11]. The couplings of photostriction, photodeformation, pyroelectricity, thermoelasticity and opto-piezothermoelasticity of two-dimensional planar opto-electromechanical photostrictive actuator were investigated by Liu and Tzou [12]. Recently, Shih and Tzou [13] developed a constitutive modeling for one- and two-dimensional distributed photostrictive actuators.

In this paper, the general opto-piezo-thermo-elastic equations for predicting behavior of photostrictive opto-electromechanical actuators are presented. All the material constants of photostrictive material are calibrated based on a laboratory experiment. A theory for the vibration control of two−dimensional elastic structures by photostrictive opto-electromechanical actuators bonded to the structure surface has been developed. This theory is applied to the vibration control of a simply supported rectangular plate using different combinations of actuators symmetrically bonded to the plate surface. In the development of smart structures, it was observed that distributed actuators, when placed symmetrically about the centerlines, have control deficiencies. One method to improve the controllability of distributed actuator is to position actuators appropriately. Since effective control depends on the location of actuators, in this paper, actuator locations are studied in order to provide good controllability and to improve actuator effectiveness.

2. An opto-electromechanical actuator

An opto-electromechanical actuator is made of photostrictive material, which is both photovoltaic—producing electricity from light—and piezoelectric—creating motion from electricity. The combination of photovoltaic and piezoelectric effects is called photostriction. Photostrictive materials are ferrodielectric ceramics that have a photostrictive effect. PLZT is a photostrictive material with the general formula [(Ph,La)(Zr,Ti)O_3] that can be used as a photostrictive actuator.

When the high-energy illumination is irradiated on the photostrictive actuator, the light causes a voltage generation between the end surface paired electrodes. This process is the photovoltaic effect. The induced photovoltaic voltage (E_l) induces actuation strains due to the converse piezoelectric effect. When illuminated, the light energy also heats up the actuator. The body temperature of the opto-electromechanical actuator rises. This temperature change then triggers the pyroelectric effect. For an opto-electromechanical actuator irradiated by high-intensity light, the induced in-plane electric field E_l(t) and the body temperature $\theta(t)$ at the time instant t_j can be estimated by [12,13]

$$E_l(t_j) = E_l(t_{j-1}) + [E_s - E_l(t_{j-1})]\frac{\alpha}{a_s} I(t_j) e^{-(\alpha/a_s)I(t_j)\Delta t}\Delta t - E_l(t_{j-1})\beta e^{-\beta\Delta t}\Delta t, \quad (1)$$

$$\theta(t_j) = \theta(t_{j-1}) + \{[I(t_j)P - \gamma\theta(t_{j-1})]\Delta t\}/(H + \gamma\Delta t), \quad (2)$$

where Δt is the time step, E_s is the saturated photovoltaic field, α is the opto-electromechanical actuator constant, β is the voltage leakage constant, P is the power of the absorbed heat, λ is the heat transfer rate, H is the heat capacity of the opto-electromechanical actuator, $I(t_j)$ is the light intensity at time t_j, and $a_s = a/b$ (length/width) is the aspect ratio.

As noted earlier, heat can trigger the pyroelectric effect from which an additional voltage is generated. The electric field $E_\theta(t)$, contributed by pyroelectric effect, can be determined from [14]

$$E_\theta(t) = \frac{P_n}{\varepsilon}\theta(t), \tag{3}$$

where P_n is the pyroelectric constant and ε is the permittivity. In view of the above discussion, the total induced electric field $E(t)$ including both the photovoltaic effect and the pyroelectric effect is

$$E(t) = E_I(t) + E_\theta(t) \tag{4}$$

The actuator strain is along its polarization direction. In general, there are two temperature-induced strain components. One is due to the thermal strain effect. The other is due to the pyroelectric effect. The photovoltaic effect and pyroelectric effect can induce a positive strain. Since heat interferes with the photostriction, the thermal effect introduces a negative strain. The total magnitude of the light-induced strains can be expressed as

$$s(t) = d_{33}E(t) - \lambda\theta(t)/Y_a \tag{5}$$

where d_{33} is the piezoelectric-strain constant, λ is a thermal stress coefficient, and Y_a is the Young's modulus of the opto-electromechanical actuator. The corresponding stress can be written as

$$T(t) = Y_a s(t) = e_{33}E(t) - \lambda\theta(t), \tag{6}$$

where e_{33} is the piezoelectric-stress constant. The expression of the actuator stress $T(t)$ is established as a function of light intensity.

3. Parameter calibration

To validate the mathematical models and the constitutive relations, photodeformation responses need to be calculated and compared with experimental data [8]. The dimensions of the clamped–free bimorph opto-electromechanical actuator used in the test are $a = 21$ mm, $b = 5$ mm and $h = 0.4$ mm. A bimorph opto-electromechanical actuator is made up of two layers of photostrictive materials as shown in Fig. 1. These two layers are arranged in opposite polarities, and the common electrodes (conducting material) are on the two end surfaces. When an illumination irradiates on one photostrictive layer, the light can induce an extensional strain and an electric field on the irradiated layer. The electric field will go through the conducting material and be applied on another layer. The voltage then triggers the converse piezoelectric effect in that layer and induce a compressive strain. In this paper, the bimorph actuator is defined in its local $(\hat{x}, \hat{y}, \hat{z})$ coordinate system.

In the experiments, ultraviolet beam is irradiated vertically to the bottom surface of the test piece, as shown in Fig. 2. The normal stress $T(t)$ in the upper layer is in compression while the lower layer is in tension. Stresses multiplied by a cross-section area gives an equivalent

force dF:

$$\mathrm{d}F = b(e_{33}E - \lambda\theta)\mathrm{d}\hat{y}. \tag{7}$$

The bending moment M can be calculated as

$$M = \int \mathrm{d}M = 2\int_0^{h_a/2} \hat{y}\mathrm{d}F = 2\int_0^{h_a/2} b(e_{33}E - \lambda\theta)\hat{y}\,\mathrm{d}\hat{y}, \tag{8}$$

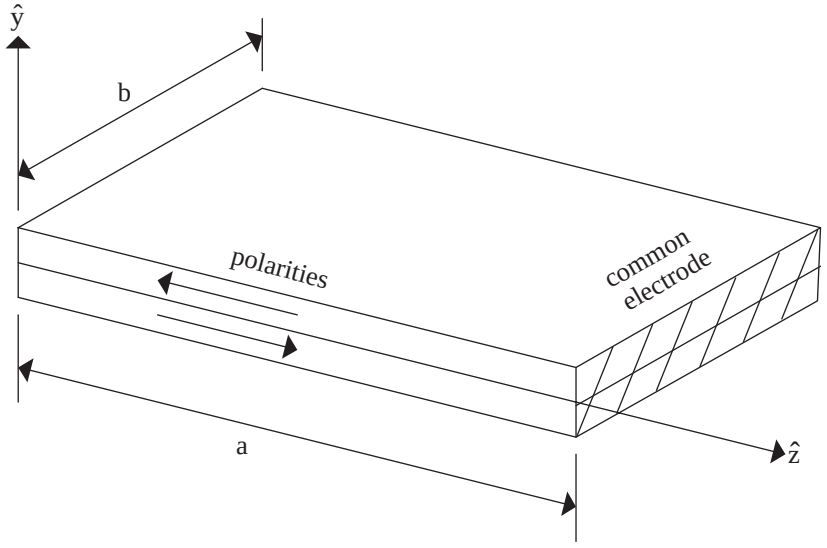

Fig. 1. Bimorph optical actuator.

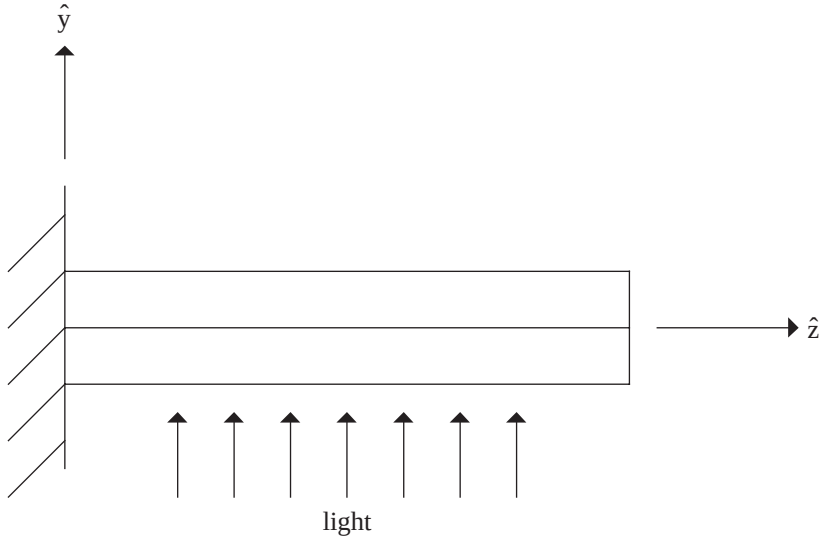

Fig. 2. Bimorph actuator under irradiation of light.

which is

$$M = (e_{33}E - \lambda\theta)\frac{bh_a^2}{4}, \tag{9}$$

where h_a is the actuator thickness. The bending moment can be related to the transverse displacement by

$$M = Y_a I \frac{\partial^2 \hat{w}}{\partial x^2}, \tag{10}$$

where I is the area moment of inertia ($I = bh_a^3/12$) and is $\hat{w}$ the transverse displacement. Hence, equating Eqs. (9) and (10) led to

$$Y_a \frac{bh_a^3}{12} \frac{\partial^2 \hat{w}}{\partial x^2} = (e_{33}E - \lambda\theta)\frac{bh_a^2}{4} \tag{11}$$

or

$$\frac{\partial^2 \hat{w}}{\partial x^2} = \frac{3(e_{33}E - \lambda\theta)}{Y_a h_a}. \tag{12}$$

Based on Eq. (12) and the boundary conditions, the transverse displacement can be derived as

$$\hat{w}(\hat{z}) = \frac{3}{2}\frac{(e_{33}E - \lambda\theta)}{Y_a h_a}\hat{z}^2. \tag{13}$$

The measured time history displacement responses at the free end are plotted in Figs. 3–5, and are compared with analytical solution calculated from Eq. (13). The surface temperature responses are also calculated and compared with experimental data reported by Fukuda et al. [8] (see Figs. 6–8). These figures demonstrate the proposed mathematical model is valid. The calibrated parameters are summarized in Table 1, which will be used for case studies.

4. Application of opto-electromechanical actuators

To demonstrate the application, two pairs of opto-electromechanical actuators are considered. The actuators are surface-bonded to a rectangular plate as shown in Fig. 9. The bonding is assumed to be infinitely thin and perfect. Since the in-plane membrane control forces and the in-plane twisting effect are usually neglected in the transverse vibration control of plates, the study here focuses on bending control effects. An actuator patch with edges defined by x_1, x_2, y_1, y_2, as shown in Fig. 9, produces a strain over its area. If the polarization of the actuator is in the x-direction, the induced bending moment in the plate can be written using unit step function $u(\cdot)$ as

$$M_{xx}^a = \frac{h + h_a}{2} h_a T(t)[u(x - x_1) - u(x - x_2)][u(y - y_1) - u(y - y_2)], \tag{14}$$

where h is the plate thickness.

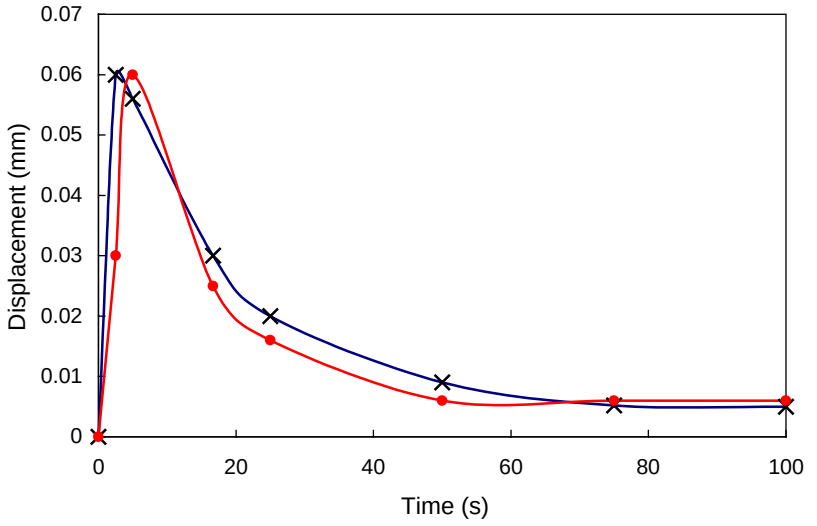

Fig. 3. Displacement response of the optical actuator for I (illumination intensity) = 200 mW/cm^2. ×, simulation; ●, experiment.

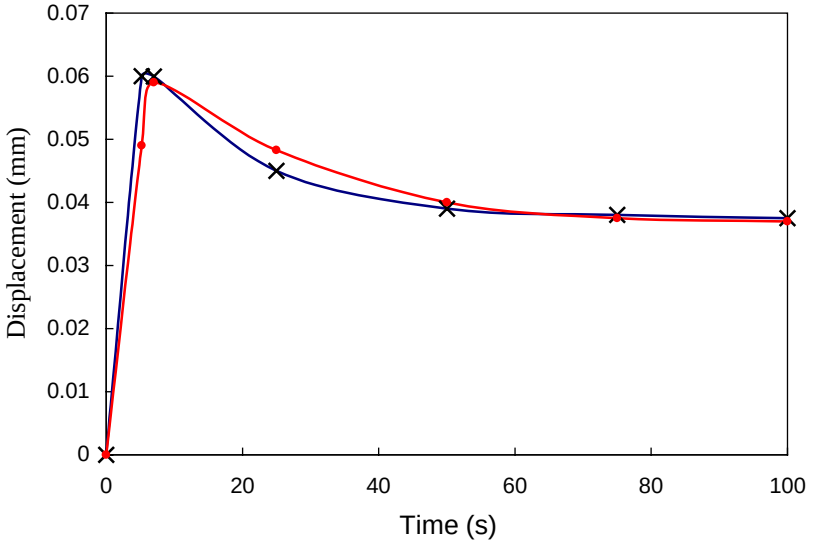

Fig. 4. Displacement response of the optical actuator for I (illumination intensity) = 100 mW/cm^2. ×, simulation; ●, experiment.

For another actuator patch, with edges x_3, x_4, y_3, y_4 and polarization in the y-direction instead of x-direction, the induced bending moment is given as

$$M^a_{yy} = \frac{h + h_a}{2} h_a T(t)[u(x - x_3) - u(x - x_4)] \cdot [u(y - y_3) - u(y - y_4)]. \tag{15}$$

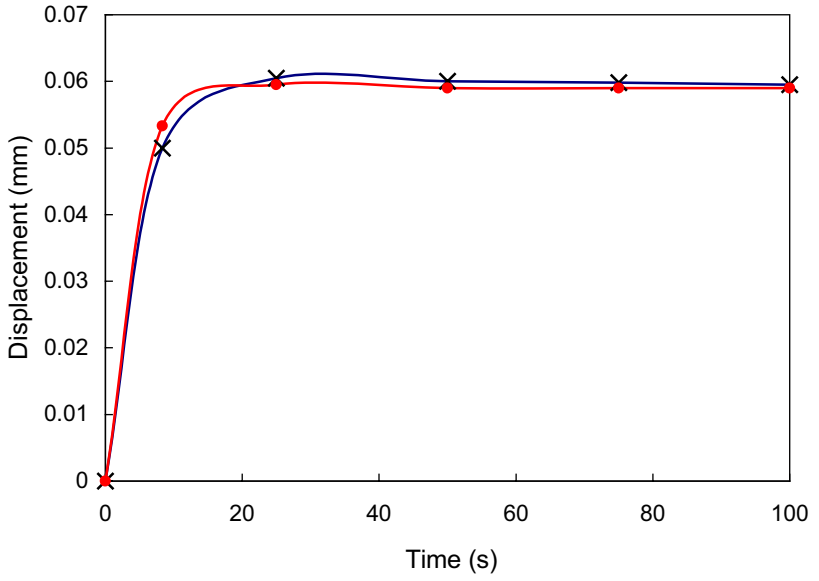

Fig. 5. Displacement response of the optical actuator for I (illumination intensity) = 25 mW/cm^2. ×, simulation; ●, experiment.

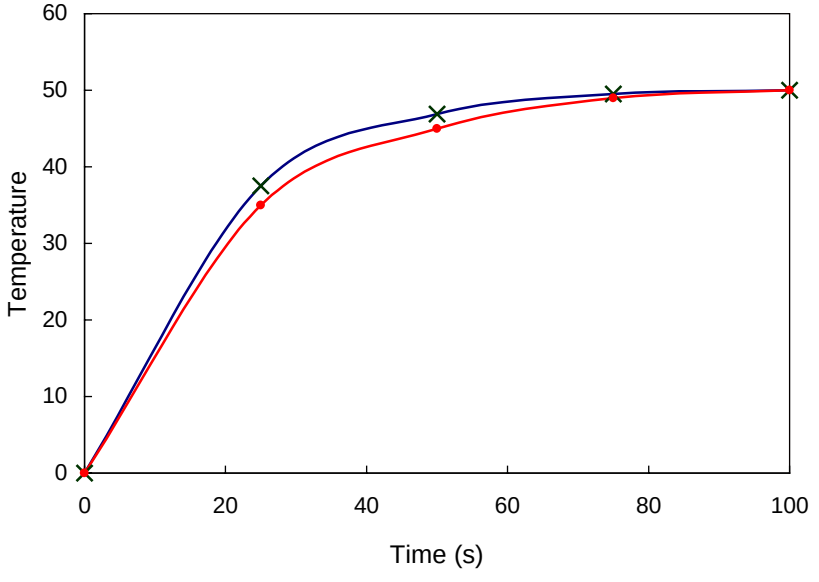

Fig. 6. Temperature response (°C) of the optical actuator for I (illumination intensity) = 200 mW/cm^2. ×, simulation; ●, experiment.

It should be pointed out that the opto-electromechanical actuators over the upper surface could cause a positive curvature of the plate. On the other hand, the actuators on the lower surface can bend the plate convex downward. Hence, the curvature is negative.

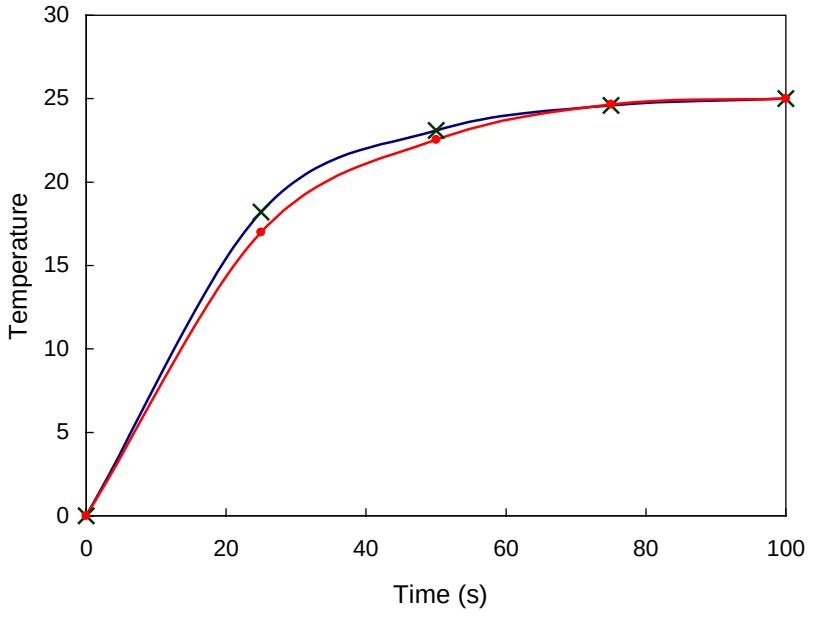

Fig. 7. Temperature response (°C) of the optical actuator for I (illumination intensity) = 100 mW/cm^2. ×, simulation; ●, experiment.

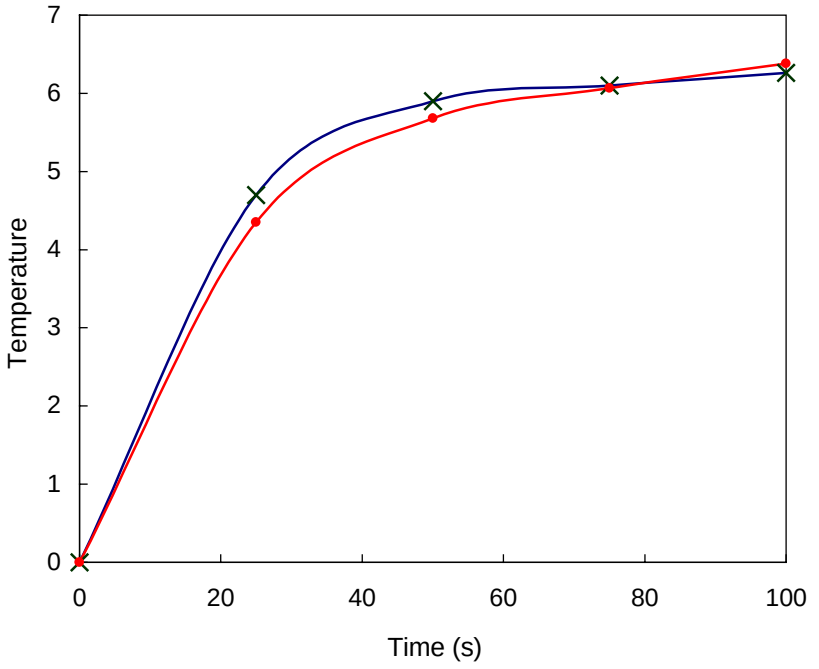

Fig. 8. Temperature response (°C) of the optical actuator for I (illumination intensity) = 25 mW/cm^2. ×, simulation; ●, experiment.

Table 1
Calibrated parameters

Variable	Value	Notes
E_s	2.43×10^5 V/m	Saturated electric field
Y_a	6.3×10^{10} N/m^2	Young's modulus
α	0.02772 cm^2/(w s)	Optical actuator constant
β	0.01 V/s	Voltage leakage constant
P	0.23×10^3 cm^2/s	Power of absorbed heat
d_{33}	1.79×10^{-10} m/V	Piezoelectric strain constant
H	16 w/°C	Heat capacity
γ	0.915 w/°C s	Heat transfer rate
λ	6.8086×10^4 N/m^2°C	Stress-temperature constant
P_n	0.25×10^{-4} C/m^2°C	Pyroelectric constant
ε	1.65×10^{-8} F/m	Electric permitivity

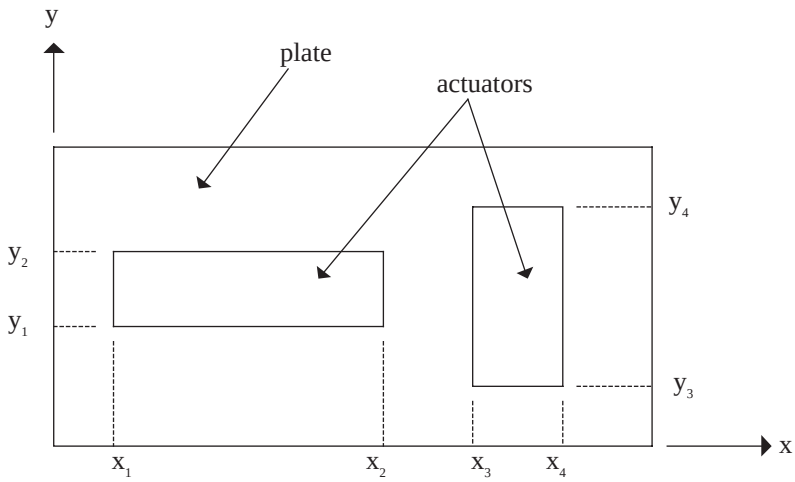

Fig. 9. Plate with opto-electromechanical actuators.

5. Dynamics of simply supported plate

For the case shown in Fig. 9, the opto-electromechanical actuators are assumed to not significantly alter the inertial mass and effective stiffness of the base plate structure. This assumption is likely to be reasonably accurate for the small and thin actuators. In view of this, the actuator mass and stiffness will not be considered in this study. It is also assumed that the plate is mechanically isotropic. Thus, the differential equation of motion takes the form

$$D\nabla^4 w + \rho h\ddot{w} = \frac{\partial^2 M^a_{xx}}{\partial x^2} + \frac{\partial^2 M^a_{yy}}{\partial y^2}, \tag{16}$$

where ∇^4 is the biharmonic operator, ρ is the mass density of the plate, and w is the plate transverse displacement. D denotes the flexural rigidity of the plate, and is defined as

$$D = \frac{Yh^3}{12(1-\mu^2)}, \tag{17}$$

where Y is the Young's modulus of the plate and μ is the Poisson's ratio.

In this study, simply supported boundary condition is assumed. The dynamic response can be written as a summation of sinusoidal modes,

$$\begin{aligned} w(x,\ y,\ t) &= \sum_{m=1}^{\infty}\sum_{n=1}^{\infty} \eta_{mn}(t) \sin\frac{m\pi x}{L_x} \sin\frac{n\pi y}{L_y} \\ &= \sum_{m=1}^{\infty}\sum_{n=1}^{\infty} \eta_{mn}(t)\phi_{nm}(x,y), \end{aligned} \tag{18}$$

where the time-dependent functions $\eta_{mn}(t)$ are the plate response amplitude of the mnth mode (or modal coordinate), and L_x and L_y are the dimensions of the plate. The symbol $\phi_{mn}(x,y)$ is used to simplify the expression.

Substituting the modal expression (18) into the system equation (16) leads to an equation in term of the modal coordinate. Integrating over the whole plate surface, applying the modal orthogonality of natural modes, the modal equation can be written as

$$\begin{aligned} \ddot{\eta}_{mn} + 2\zeta_{mn}\omega_{mn}\dot{\eta}_{mn} + \omega_{mn}^2\eta_{mn} = {} & \frac{4}{\rho h L_x L_y}\int_x\int_y \frac{\partial^2 M_{xx}^a}{\partial x^2}\phi_{mn}(x,y)\,\mathrm{d}x\,\mathrm{d}y \\ & + \frac{4}{\rho h L_x L_y}\int_x\int_y \frac{\partial^2 M_{yy}^a}{\partial y^2}\phi_{mn}(x,y)\,\mathrm{d}x\,\mathrm{d}y \end{aligned} \tag{19}$$

where ζ_{mn} is the damping ratio, and ω_{mn} is the natural frequency of the mnth mode.

The substitution of Eq. (14) into the first term on the right-hand side of Eq. (19) permits this term to be rewritten as

$$\begin{aligned} & \frac{4}{\rho h L_x L_y}\int_x\int_y \frac{\partial^2 M_{xx}^a}{\partial x^2}\phi_{mn}(x,\ y)\mathrm{d}x\,\mathrm{d}y \\ & = \frac{-2(h+h_a)h_a T}{\rho h L_x L_y}\int_x\int_y \frac{\partial^2}{\partial x^2}([u(x-x_1)-u(x-x_2)]\cdot[u(y-y_1)-u(y-y_2)])\,\phi_{mn}(x,\ y)\mathrm{d}x\,\mathrm{d}y \\ & = \frac{-2(h+h_a)h_a T}{\rho h L_x L_y}\left(\frac{mL_y}{nL_x}\right)\left[\left(\cos\frac{m\pi x_1}{L_x}-\cos\frac{m\pi x_2}{L_x}\right)\left(\cos\frac{n\pi y_1}{L_y}-\cos\frac{n\pi y_2}{L_y}\right)\right] \\ & = -\tilde{M}_{mnx}. \end{aligned} \tag{20}$$

With reference to the third line of above equation, it should be pointed out that the first part in Eq. (20) is related to material, geometry and the induced stress, whereas the second part is modal and dimension dependent, and the third part defines the spatial characteristics. Similarly, an

insertion of Eq. (15) into the second term on the right-hand side of Eq. (19) yields

$$\begin{aligned}
&\frac{4}{\rho h L_x L_y}\int_x\int_y \frac{\partial^2 M^a_{yy}}{\partial y^2}\,\phi_{mn}(x,\,y)\mathrm{d}x\,\mathrm{d}y\\
&=\frac{-2(h+h_a)h_a T}{\rho h L_x L_y}\int_x\int_y \frac{\partial^2}{\partial y^2}\left([u(x-x_3)-u(x-x_4)]\cdot[u(y-y_3)-u(y-y_4)]\right)\phi_{mn}(x,\,y)\mathrm{d}x\,\mathrm{d}y\\
&=\frac{-2(h+h_a)h_a T}{\rho h L_x L_y}\left(\frac{nL_x}{mL_y}\right)\left[\left(\cos\frac{m\pi x_3}{L_x}-\cos\frac{m\pi x_4}{L_x}\right)\left(\cos\frac{n\pi y_3}{L_y}-\cos\frac{n\pi y_4}{L_y}\right)\right]\\
&=-\tilde{M}_{mny}. \qquad (21)
\end{aligned}$$

The symbols $\tilde{M}_{mnx}$ and $\tilde{M}_{mny}$ are used to simplify the expressions and will be used later in the paper.

In this study, the opto-electromechanical actuators are, respectively, placed on the top and bottom surfaces of the plate. In this way, when the light is applied to one surface, the surface bonded actuator induces a positive control action. However, when the light irradiates on the surface of another actuator, the control action is negative. Thus, by alternately activating the light sources, both positive and negative control actions can be generated for vibration control of the plate. In view of this, Eq. (19) can be rewritten as

$$\ddot{\eta}_{mn}+2\zeta_{mn}\omega_{mn}\dot{\eta}_{mn}+\omega^2_{mn}\eta_{mn}+\mathrm{sgn}(\dot{\eta}_{mn})(\tilde{M}_{mnx}+\tilde{M}_{mny})=0, \qquad (22)$$

where the symbol "sgn" denotes "sign of" and represents a function having value $+1$ if the argument $\dot{\eta}_{mn}$ is positive and value -1 if its argument is negative.

In this study, constant light intensity control is used. The light intensity $I(t)$ can be expressed as

$$I(t)=G[\max|\dot{\eta}_{mn}(t)|], \qquad (23)$$

where G is the feedback gain.

6. Case study

Based on the modeling of the opto-electromechanical actuator and its coupling with an elastic plate, dynamics and control effectiveness are investigated in this section. Results are presented for the active vibration control of a plate with opto-electromechanical actuators. The dimensions of the plate is $L_x = 0.8\,\mathrm{m}$, $L_y = 0.6\,\mathrm{m}$ and $h = 1.0\,\mathrm{mm}$. The opto-electromechanical actuators with thickness of 0.25 mm are applied over the upper and lower surfaces for control of vibration of the plate. The plate was assumed to be steel with material properties given as $Y = 2.1\times10^{11}\,\mathrm{N/m^2}$ and $\rho = 7.8\times10^3\,\mathrm{kg/m^3}$. The material properties of actuator are taken as $Y_a = 6.3\times10^{10}\,\mathrm{N/m^2}$, and $\rho_a = 7.6\times10^3\,\mathrm{kg/m^3}$. In this study, in order to show clearly the effects of active damping, structural damping is not taken into account.

In this study, two different configurations of actuators are investigated and their layout is given in Fig. 10. For configuration *I*, three actuators were symmetrically placed at the center of each plate surface. In the second arrangement, two actuators were placed at $x_1 = 0.05\,\mathrm{m}$, $x_2 = 0.29\,\mathrm{m}$,

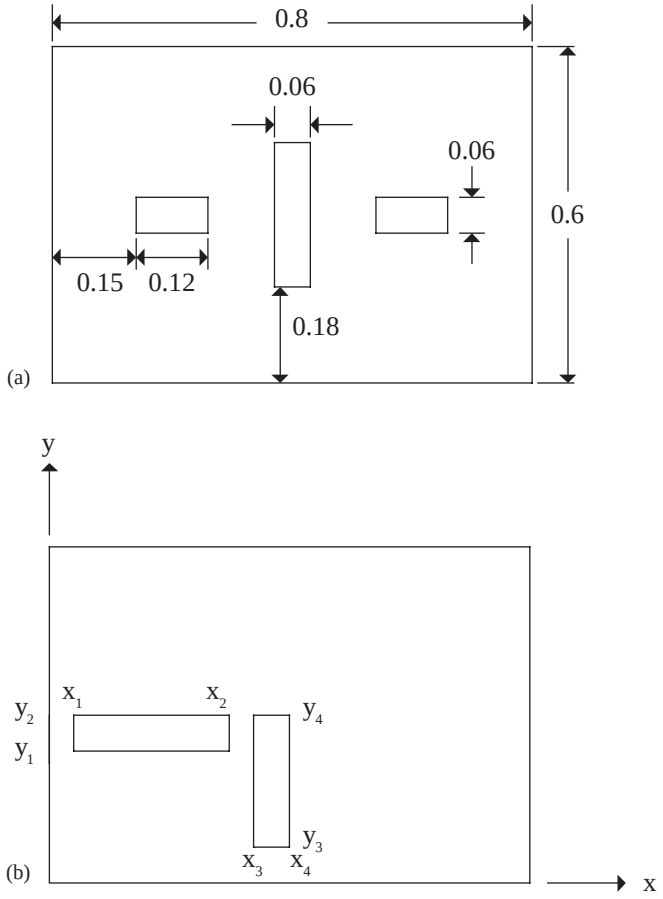

Fig. 10. (a) Test configuration I; (b) test configuration II.

$y_1 = 0.24\,\text{m}$, $y_2 = 0.3\,\text{m}$, $x_3 = 0.34\,\text{m}$, $x_4 = 0.4\,\text{m}$, $y_3 = 0.06\,\text{m}$, $y_4 = 0.30\,\text{m}$, respectively, on both sides of the plate.

In this work, the analytical model is approximate since the mass and stiffness of the actuators are not considered. To study the effect of the actuator patches on the dynamic response of plates, a finite element model is developed. The finite element model was validated by comparing its predictions with the exact natural frequencies of simply supported plates. The exact frequencies can be determined by the formula

$$\omega_{mn} = \pi^2 \sqrt{\frac{D}{\rho h}} \left[\left(\frac{m}{L_x} \right)^2 + \left(\frac{n}{L_y} \right)^2 \right]. \tag{24}$$

The first four natural frequencies of plates (exact values and the values predicted by the FE method) are tabulated in Table 2. The frequencies for the plate with bonded actuator patches (Configuration I) are also computed and presented in Table 2. It is seen from this table that the

presence of the photostrictive patches leads to an increase in the natural frequencies of the plates. Overall, the frequency changes are less than 2% that are practically insignificant.

The presence of actuator patches can increase the stiffness of the plate system. To further investigate the effect of stiffness of the photostrictive patches, a static comparison has been performed. Finite element analyses are applied to the plate without and with photostrictive actuators. The geometry for the plate with bonded actuators is illustrated in Fig. 10(a). The plate is subject to a uniform load of 100 Pa. The variations of the transverse deflection (along the $L_y/2$ line) are shown in Fig. 11. From this figure, it can be seen that disparities are present. However, the added actuator stiffness still does not significantly alter the stiffness of the plate. Based on the above analyses, it can be seen that the developed mathematical model, although approximate (neglecting the effects of the patches), suffices for the present study.

Table 2
Natural frequencies of the simply-supported plate models

Modal indices	Natural frequencies (Hz)		
	Exact (without patch)	FE (without patch)	FE (with patches)
(1,1)	10.7050	10.6435	10.8028
(2,1)	22.2665	22.0293	22.2811
(1,2)	31.2587	30.9893	31.3219
(2,2)	42.8202	41.9970	42.1448

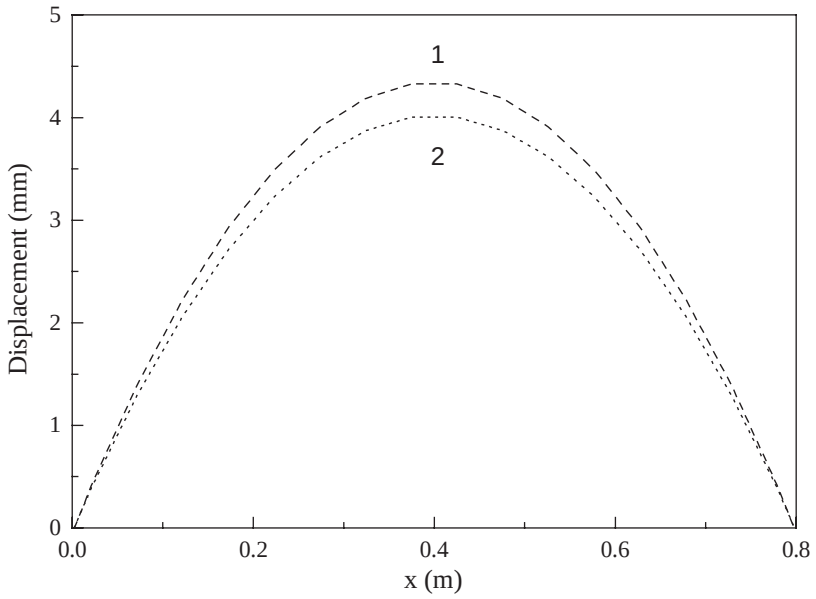

Fig. 11. Displacements at $y = L_y/2$ for the plates with and without photostrictive actuator patches. – – – – –, without patch; - - - - -, with patch.

6.1. Configuration I

The center of the plate is the location of the highest strain for the (1,1) mode. When the actuators are placed at this location, the control effectiveness is greater. It is apparent from Fig. 12 that the (1,1) mode is completely controlled and the modal amplitude is effectively suppressed within 1.5 s. As far as the (2,1) mode is concerned, the actuator is located symmetrically across the (2,1) nodal line at $L_x/2$. The parallel actuator edges cancel each other. The modal amplitude in this case, Fig. 13, shows that the (2,1) mode is uncontrollable. As can be seen from Fig. 14, for this location of the actuators, the (1,2) mode also cannot be controlled. From the results of Figs. 12–14, it appears that the centrally located actuators can control the symmetric modes ($m = 1, 3, 5, \ldots$; $n = 1, 3, 5, \ldots$) while the asymmetric modes ($m = 2, 4, 6, \ldots$; $n = 2, 4, 6, \ldots$) are not controlled at all.

6.2. Configuration II

From the above results, it is clear that in order to ensure the controllability for most of the vibration modes, the actuators need to be placed unsymmetrically about the $L_x/2$ and $L_y/2$ lines. Figs. 15–17 show the modal amplitude of the (1,1), (2,1) and (1,2) modes, respectively, for this configuration. With reference to Figs. 12 and 15, it is observed that when the actuators is in configuration II, the control effect is low as compared to the configuration I. However, analysis of Figs. 16 and 17 reveals that this arrangement provides good control effect over the asymmetric modes. Hence, the overall controllability can be improved. This increased effectiveness is attributed to the actuators' being in the better locations for controlling most of the structural vibration modes.

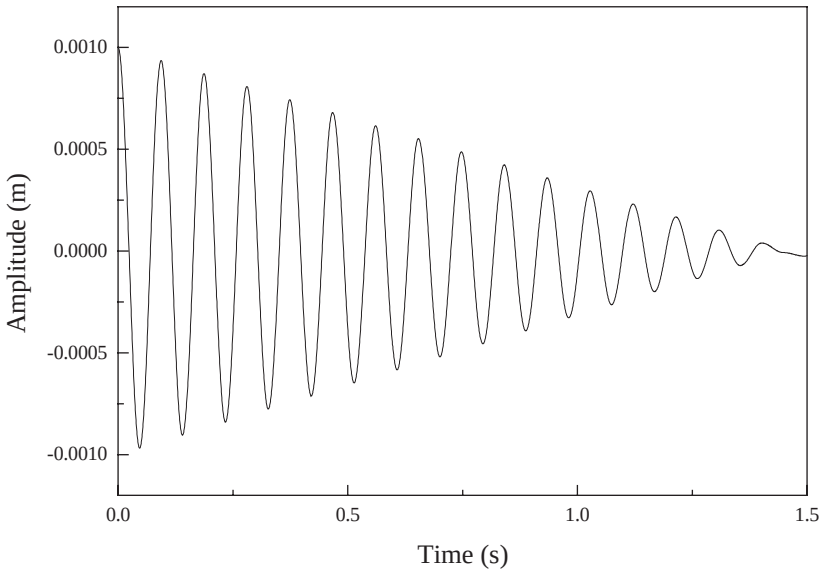

Fig. 12. Mode (1,1) response, Configuration I.

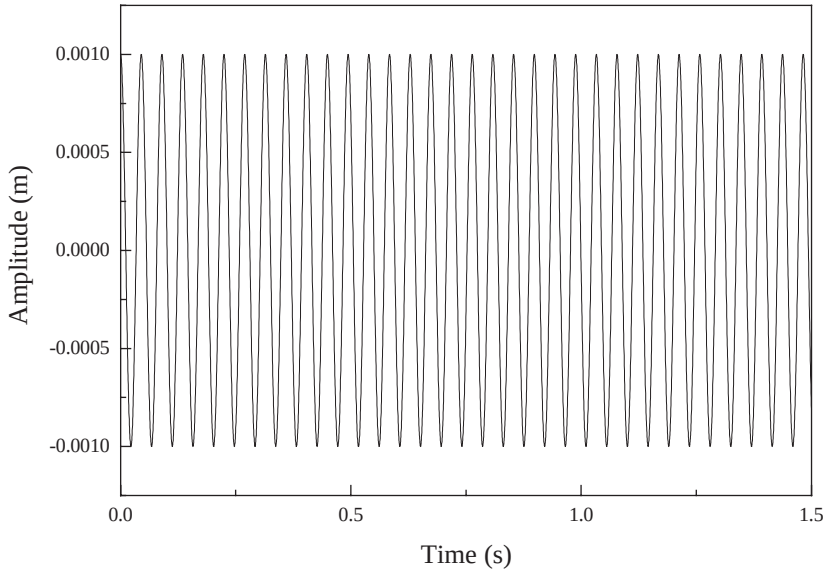

Fig. 13. Mode (2,1) response, Configuration I.

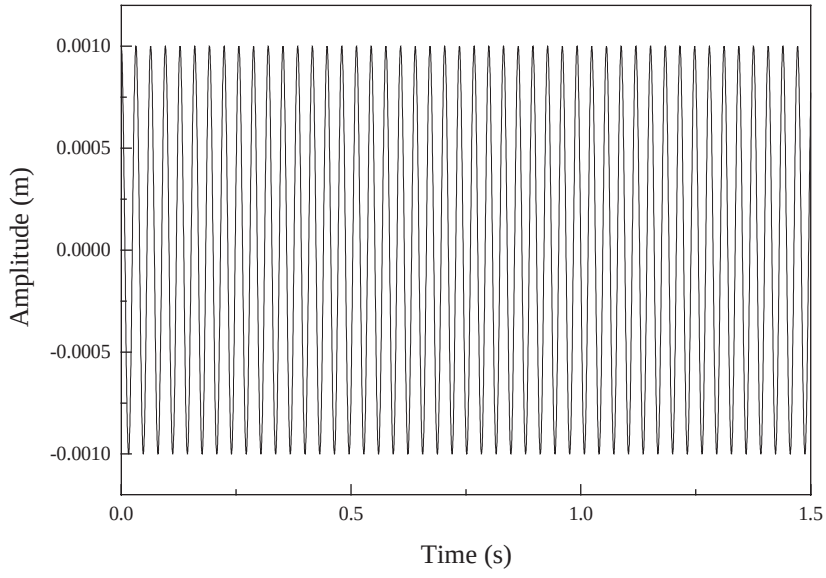

Fig. 14. Mode (1,2) response, Configuration I.

The results of this study reveal that effective control depends on the locations of actuators. In order to utilize the advantage of photostrictive transducers and maximize actuator effectiveness, it is necessary to select appropriate positions of the transducers. The positions of the structure at which the strain is highest are the best locations for actuators. Therefore, the actuators should be placed in the regions of high average strains and away from areas of zero strains (nodal line).

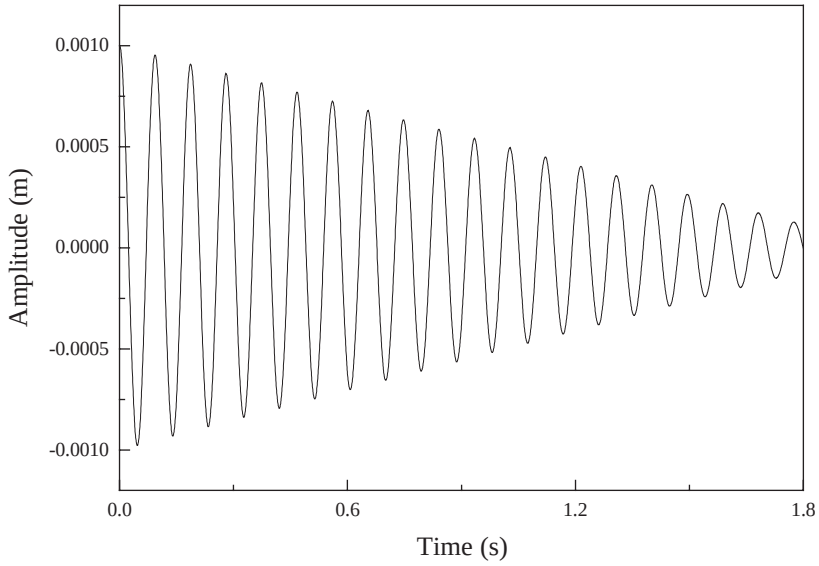

Fig. 15. Mode (1,1) response, Configuration II.

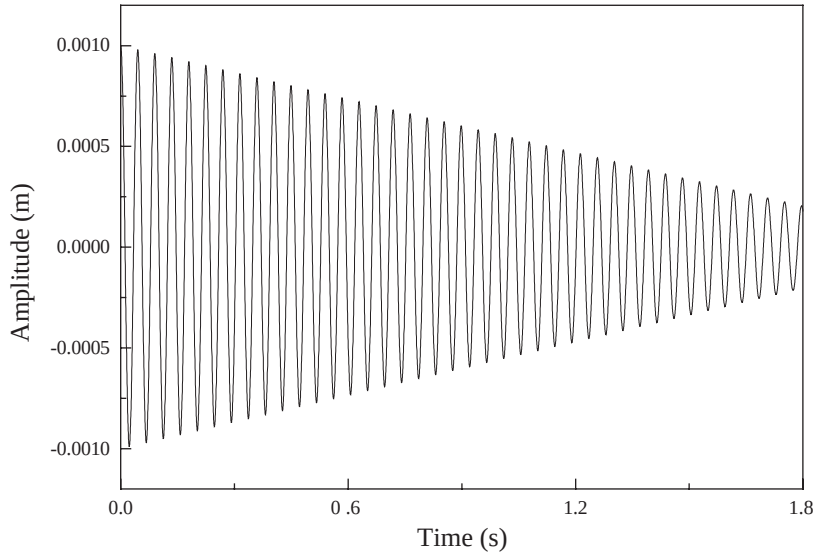

Fig. 16. Mode (2,1) response, Configuration II.

7. Conclusions

This paper presents an analytical modeling for active vibration control of a flexible simply supported plate structure by opto-electromechanical actuators. Based on the fundamental photostrictive material properties, which include elastic, electric, light and temperature fields, the

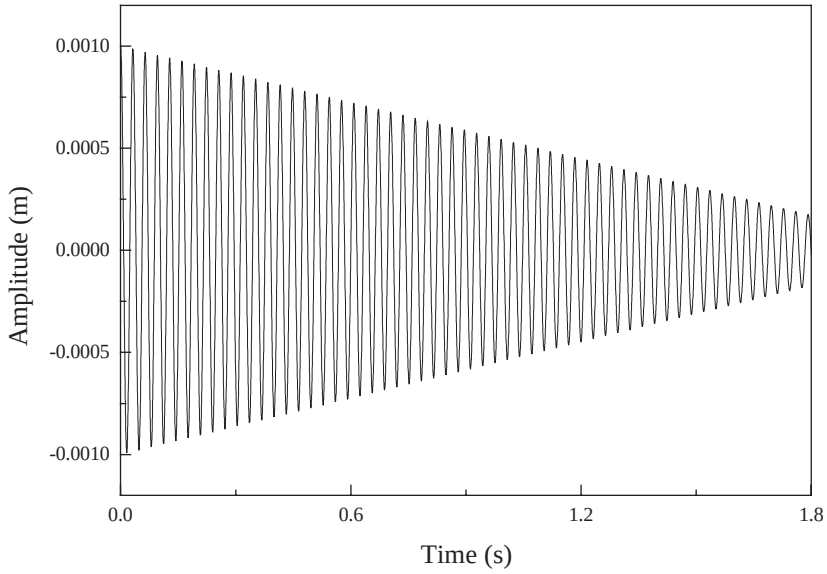

Fig. 17. Mode (1,2) response, Configuration II.

formulation of induced stress is derived. In the following, this multi-field coupled model is applied to distributed vibration control.

The opto-electromechanical actuators are only capable of actuation along one direction. In order to control a plate, two or more actuator pairs are needed. The placement of actuators is one of the main problems in the design of adaptive/smart structures. The location of actuator strongly influences the effectiveness of the actuator to control certain modes. With the knowledge of mode shape of the plate structure and the photostrictive actuator behavior, one can select better actuator positions on the plate to maximize the vibration controllability. In this paper, vibration control effects of two different actuator layouts are studied. The results obtained from the case study indicate that the use of an array of appropriately positioned actuators can provide good controllability of the structure. The results presented in this study also can provide a better understanding of opto-electromechanical actuator and control behavior of smart photostrictive structronic systems.

It should be noted that the speed of response of the photostrictive actuators is not very fast compared with the piezoelectric actuators. A study [15] shows that the photostrictive response can reach around 100 Hz actuation frequency. Hence, the photostrictive actuators are effective in static and low-frequency dynamic applications. For high-frequency applications, this type of actuators may not be very effective. However, light-driven opto-electromechanical actuators have many advantages over traditional electromechanical actuators, such as remote actuation and immunity from electric/magnetic disturbances. Therefore, the detailed opto-electro-mechanics need to be investigated. The practical applications of this type of actuators need to be investigated. The practical applications of this type of actuators need to be explored. Further study in this area is underway, the results of which will be presented subsequently.

Acknowledgements

The supports of the US Army Tank-automotive and Armaments Command (TACOM) and the National Aeronautics and Space Administration (NASA) are gratefully acknowledged.

References

[1] A. Baz, S. Poh, A new class of distributed sensors, *Journal of Vibration and Acoustics* 119 (1997) 582–589.
[2] S.Y. Wang, S.T. Quek, K.K. Ang, Vibration control of smart piezoelectric composite plates, *Journal of Smart Materials and Structures* 10 (2001) 637–644.
[3] H.S. Tzou, G.L. Anderson, *Intelligent Structural Systems*, Kluwer Academic Publishers, Boston, 1992.
[4] K. Uchino, *Piezoelectric Actuators and Ultrasonic Motors*, Kluwer Academic Publishers, Boston, 1996.
[5] Senol Utku, *Theory of Adaptive Structures, Incorporating Intelligence into Engineered Products*, CRC Press, Boca Raton, FL 1998.
[6] Y. Wang, J.C. Slater, A comparison of conventional and impedance methods for modeling piezoelectric materials actuation in smart structures, *Journal of Vibration and Acoustics* 120 (1998) 685–688.
[7] Hui-Ru Shih, Distributed vibration sensing and control of a piezoelectric laminated curved beam. *Journal of Smart Materials and Structures* 9 (2000) 761–766.
[8] T. Fukuda, S. Hattori, F. Arai, H. Matsuura, T. Hiramatsu, Y. Ikeda, A. Maekawa, Characteristics of optical actuator – servomechanisms using bimorph optical piezoelectric actuator, *Proceedings of 1993 IEEE Robotics and Automation Conference*, 1993, pp. 618–623.
[9] K. Uchino, Photostrictive Actuators, *Proceedings of 1990 IEEE Ultrasonics Symposium*, 1990, pp. 721–723.
[10] P.S. Brody, Optomechanical bimorph actuator, *Ferroelectrics* 50 (1983) 27–32.
[11] K. Uchino, New applications of photostriction, *Innovations in Materials Research* 1 (1996) 11–22.
[12] B. Liu, H.S. Tzou, Distributed photostrictive actuation and opto-piezothermoelasticity applied to vibration control of plates, *Journal of Vibration and Acoustics* 120 (1998) 937–943.
[13] Hui-Ru Shih, H.S. Tzou, Opto-piezothermoelastic constitutive modeling of a new 2-d photostrictive composite plate actuator, *Proceedings of ASME IMECE* 61 (2000) 1–8.
[14] T.R. Tauchert, Piezothermoelastic behavior of laminated plate, *Journal of Thermal Stresses* 15 (1992) 25–37.
[15] S.Y. Chu, K. Uchino, Photoacoustic devices using PLZT ceramics, *Proceedings of IEEE International Symposium on Applied Ferroelectrics*, 1994.